

UC Office of the President

UC Lab Fees Research Program (LFRP) Funded Publications

Title

Enhanced interlayer neutral excitons and trions in trilayer van der Waals heterostructures

Permalink

<https://escholarship.org/uc/item/5wn3m1s9>

Author

Wong, Chee Wei

Publication Date

2019-01-08

Peer reviewed

Enhanced interlayer neutral excitons and trions in trilayer van der Waals heterostructures

Chanyeol Choi^{1,2,†}, Hung-Chieh Cheng^{3,4}, Hyunseok Kim², Abhinav Kumar Vinod^{1,2}, Sang-Hoon Bae^{3,4}, V. Ongun Özçelik⁵, Roberto Grassi⁶, Jongjae Chae³, Shu-Wei Huang^{1,2}, Xiangfeng Duan^{4,7}, Kristen Kaasbjerg⁸, Tony Low⁶, and Chee Wei Wong^{1,2,†}

¹ Fang Lu Mesoscopic Optics and Quantum Electronics Laboratory, University of California, Los Angeles, CA 90095, United States

² Department of Electrical Engineering, University of California, Los Angeles, CA 90095, United States

³ Department of Materials Science and Engineering, University of California, Los Angeles, CA 90095, United States

⁴ California Nanosystems Institute, University of California, Los Angeles, CA 90095, United States

⁵ Andlinger Center for Energy and the Environment, Princeton University, Princeton, New Jersey 08544, United States

⁶ Department of Electrical and Computer Engineering, University of Minnesota, Minneapolis, MN 55455, United States

⁷ Department of Chemistry and Biochemistry, University of California, Los Angeles, CA 90095, United States

⁸ Center for Nanostructured Graphene (CNG), Department of Micro- and Nanotechnology (DTU Nanotech), Technical University of Denmark, DK-2800 Kgs. Lyngby, Denmark

† Corresponding authors: cowellchoi@gmail.com ; cheewei.wong@ucla.edu

Vertically stacked van der Waals heterostructures constitute a promising platform for providing tailored band alignment with enhanced excitonic systems. Here we report the first observations of neutral and charged interlayer excitons in trilayer WSe₂-MoSe₂-WSe₂ van der Waals heterostructures and their dynamics. The addition of a WSe₂ layer in the trilayer leads to significantly higher photoluminescence quantum yields and tunable spectral resonance compared to its bilayer heterostructures at cryogenic temperatures. The observed enhancement in the photoluminescence quantum yield is due to significantly larger electron-hole overlap in the trilayer heterostructure, supported via first-principle pseudopotential calculations based on spin-polarized density functional theory. We further uncover the temperature- and power-dependence, as well as time-resolved photoluminescence of the trilayer heterostructure interlayer neutral excitons and trions. Our study elucidates the prospects of manipulating light emission from interlayer excitons and designing atomic heterostructures from first-principles for optoelectronics.

Keywords: transition metal dichalcogenides; heterostructures; exciton; trion; spectroscopy.

In two-dimensional (2D) materials, Coulomb-induced electronic states of excitons have been examined as a platform to understand many-body carrier-carrier interactions. These excitonic interactions dominate in layered materials due to quantum confinement and reduced dielectric screening. 2D atomic crystals of transition metal dichalcogenides (TMDs) have provided new opportunities in the studies of single-exciton single-photon interactions, spin-orbit coupling, ultrafast dynamics, and nanoelectronic devices [1-22]. Layer-by-layer stacking of TMDs-based van der Waals (vdWs) heterostructures has recently captured the attention of the scientific community where the tailored band alignment with diverse 2D materials can be achieved via advanced 2D growth and transfer techniques [23-28]. This has allowed the extension of indirect excitons with spatially separated electrons and holes from, for example, coupled quantum wells in GaAs/AlGaAs [29,30] to TMD vdW heterostructure bilayers, where they are referred to as interlayer excitons. These interlayer excitons exhibit rich physics in TMDs-based vdWs heterostructures due to the novel atomic granularity control through layer-by-layer stacking and the chiral properties of quantum electronic states [8,31,32]. Recently several studies observed that interlayer excitons feature long lifetimes, spin-valley polarization by circularly-polarized pumping, and charge transfer at the heterogeneous interfaces [32-42].

Here we demonstrate for the first time TMDs-based vdWs heterostructures composed of a three-layer $\text{WSe}_2\text{-MoSe}_2\text{-WSe}_2$ stack to achieve unique band alignment that promotes efficient interlayer radiative recombination. We first design the heterostructure through pseudopotential calculations based on spin-polarized density functional theory, with the exchange-correlation potential estimated via the Perdew-Burke-Ernzerhof functional. Optimizing the designed heterostructure band structure through conjugate gradients, we include the effects of spin-orbit coupling through non-collinear computations. We correlate the obtained real-space pseudo-wavefunctions with lattice points in reciprocal space to understand the carrier localization, the type-II optical transition oscillator strength, and potential asymmetries in the electron and hole band profiles towards neutral interlayer excitons and three-body trion complexes. Enabled by the first-principle computations, we fabricate the trilayer heterostructure stack through hexagonal boron nitride assisted transfer. Our dry transfer process allows a relatively undoped heterostructure and atomic smoothness at the interfaces. We perform cryogenic photoluminescence on the designed trilayer heterostructure along with time-resolved pulsed measurements via time-correlated single-photon counting, mapping the spectral, pump fluence and bath temperature dependence of the interlayer excitons. We observe an order-of-magnitude larger photoluminescence in the trilayer compared to bilayer heterostructures, due to the more distributed hybridized valance band state in the trilayer for

increased oscillator strength, along with the formation of the neutral interlayer exciton. At 4K we observe a spectrally-distinguishable trion formation. We determine that the energy splitting between the neutral exciton and trion is largely dependent on the pump fluence and photocarrier densities instead of the bath temperature. We observe that the trion mostly red-shifts while the neutral exciton stays consistent, and extract a trion binding energy of approximately 27 meV in our trilayer heterostructure. With increasing photocarrier injection and decreasing bath temperatures, the trion-to-neutral intensity ratio is also increased. Radiative lifetimes of the interlayer excitons are measured up to ≈ 2.54 ns at 4K. We examine the radiative lifetimes for different bath temperatures, pump fluences and excitation wavelengths, with observed stronger dependences on the bath temperature. Our study enables the engineering of indirect neutral excitons and charged trions with spatially separated electron and hole wavefunctions, towards control of the oscillator strengths and excitonic character with designed atomic granularity

MATERIALS AND METHODS

Computational method:

In the computational modeling of the MoSe₂ and WSe₂ based heterostructures, the atomic structure of monolayer MoSe₂ and WSe₂ are first optimized using first-principles pseudopotential calculations based on the spin-polarized density functional theory (DFT) within the generalized gradient approximation (GGA). The optimized monolayers are placed on top of each other with proper interlayer distances that correspond to the ground state energy for each heterostructure. During this process, van der Waals corrections are implemented following the DFT-D2 method of Grimme [48]. Projector-augmented wave potentials (PAW) [49] are used in the calculations and the exchange-correlation potential is approximated with Perdew-Burke-Ernzerhof functional [50]. During the geometrical optimization steps, the Brillouin zone (BZ) is sampled in the Monkhorst-Pack scheme, where the convergence in energy as a function of the number of k -points is tested. The k -point sampling of (21×21×1) is found to be suitable for the BZ corresponding to the primitive MoSe₂ and WSe₂ unit cells. The heterostructures are optimized using the conjugate gradient method, where the total energy and atomic forces are minimized. The energy convergence value between two consecutive steps is chosen as 10^{-5} eV. A maximum force of 0.01 eV/Å is allowed on each atom. In order to avoid interactions between periodic unit cells, a supercell with 20 Å vacuum is used. The optimized heterostructures are then used for the electronic band structure calculations. The band diagrams are obtained by calculating the energies at 150 k -points between the Γ -M-K- Γ high symmetry points in the BZ. The effects of spin-orbit coupling on the electronic structures are calculated by

performing non-collinear computations as implemented in VASP [51]. The real-space wavefunctions are obtained from the DFT calculations using the binary wavefunction file that is produced by VASP. The binary WAVECAR file that is produced after a series of DFT calculations at the K-point is then mapped by WaveTrans, which correlates the binary wavefunctions with the corresponding lattice points in the reciprocal space and their associated planewave coefficients. The real-space pseudo-wavefunction is constructed again using WaveTrans [52].

Sample preparation and characterization:

Single-layer (SL) MoSe₂ and SL WSe₂ flakes are separately prepared by mechanical exfoliation on clean 290 nm SiO₂/Si substrates. A thin layer of hexagonal boron nitride is first exfoliated on a PMMA/PPC stack, which is then used for layer-by-layer picking up of the prepared WSe₂ and MoSe₂ in order. The picked up MoSe₂/WSe₂/h-BN/polymer stack is finally transferred on a WSe₂/SiO₂/Si substrate [25,26]. During the entire dry transfer process, no solvent is involved to ensure the atomically clean interface between the 2D materials. Raman measurement (Renishaw, inVia basis) is conducted using a 532 nm laser to map out the sample quality.

Cryogenic micro-photoluminescence and time-resolved photoluminescence:

We use an optical cryostat (Janis Research ST-100) to measure the cryogenic photoluminescence at 4 K. Measurements are carried out using a Si detector (Newport Model 2151) for the shorter wavelength regime (400 nm to 1000 nm) with a continuous-wave He-Ne 632.8 nm pump laser. For the longer wavelengths (900 nm to 1600 nm) where interlayer exciton and trion can exist, an InGaAs focal plane array detector with liquid nitrogen cooling system (Princeton Instruments 2D-OMA) is used with high responsivity. The detector signal is improved by using a lock-in amplifier and selectively filtered by a spectrometer (Princeton Instruments SpectraPro 2500i). TRPL measurements are performed using a time-correlated single-photon counting (TCSPC) system with PicoQuant. The sample is excited with a 30 ps 39/78 MHz tunable pulse laser system (NKT Photonics SuperK EXTREME EXW-12) and detected with a single-photon counting module (SPCM-AQR-16) attached to a monochromator and processed by a PicoHarp 300 correlating system with ≈ 300 ps resolution. The TRPL measurements are conducted at low temperature with optical filters in an enclosed optical setup to prevent pump and stray ambient light from affecting the detectors.

RESULTS AND DISCUSSION

Theoretical analysis:

Here we introduce the concept towards the enhancement of the exciton recombination rate of the trilayer heterostructure illustrated in Figure 1a-b. The trilayer heterostructure consists of a single-layer (SL) MoSe₂ sandwiched between two SLs of WSe₂. The anticipated type-II band alignment, depicted in Figure 1b, supports excitons with the electron and hole residing respectively in the conduction band of MoSe₂ and valence band of WSe₂. This resembles the situation for excitons in heterostructure bilayers, where the electron and hole are strongly localized to the different layers by the large band offsets [53-55]. This is indeed the case for the electron in the conduction band of the trilayer structure, which is strongly localized in the central MoSe₂ layer due to a weak interlayer coupling [56]. However, in our case, the valence band states are subject to a stronger interlayer coupling [56]. Consequently, the valence band states in our two outer WSe₂ layers hybridize with the state in the central MoSe₂ layer. Accordingly, the delocalization of the valence band state over the entire trilayer enables the strong overlap of the electron-hole in the trilayer, compared to the prior bilayer counterparts.

To support this physical picture, we carried out first-principles density functional theory (DFT) calculations including the spin-orbit interaction of the bilayer and trilayer band structures and wavefunctions, with the computational details described in the above Methods. The results are summarized in Figures 1c and 1d. (Band structures of SL MoSe₂ and SL WSe₂ are shown in Supplementary Section S1.) While the bilayer heterostructure shows a ≈ 1.22 eV bandgap, the trilayer heterostructure has a slightly smaller ≈ 1.21 eV bandgap, both at the K-point. In both the bilayer and trilayer structures, our calculations predict states which are predominantly localized in either WSe₂ (blue) or MoSe₂ (red) layers, in agreement with the band alignment illustrated in Figure 1b. Figure 1e and 1f show the spatial distribution profile of the electron and hole probability densities in the out-of-plane direction, for the states at the valence and conduction band edges. In the bilayer the electron and hole states hardly overlap, hence the long lifetime [31,32,57,58], and our weaker PL shown in Figure S3. On the other hand, in the trilayer structure the valence band state shows the expected delocalization with a large center-layer component and thus a significant overlap with the localized conduction band state.

In our proposed scheme as shown in Figure 1b, the type-II staggered heterojunction leads to energetically lower excitonic states due to the band offset between MoSe₂ and WSe₂. Furthermore, with the trilayer heterostructure, the strong asymmetry between the electron and hole band profile promotes excitons complexes such as trions [2,16,33,39,59]. Unlike bilayer

TMD heterostructures, a metallic state through biasing the Fermi level in the conduction or valence band is required in the trilayers to produce imbalance in electron and hole populations and hence increase the likelihood of trions formation [33,39]. The interlayer trions can be achieved, for example, with two electrons in the MoSe₂ layers and one hole in the WSe₂ layer. A description of the radiative recombination pathways in the trilayer and the trions is shown in Supplementary Section S2.

Experimental results and discussion:

We fabricate the WSe₂-MoSe₂-WSe₂ trilayer heterostructure on a SiO₂/Si substrate by dry transfer with a hexagonal boron nitride (*h*-BN) flake of 20 nm thickness as shown in Figure 2a. Both SL WSe₂ and SL MoSe₂ are mechanically exfoliated from bulk crystals and identified with optical microscopy, PL and Raman spectra. Before the stacking process, the sample thickness is further confirmed independently via atomic force microscopy (AFM) as shown in Figure 2b. Raman spectroscopy is conducted on the SL MoSe₂, SL WSe₂, 20 nm-thick *h*-BN as well as TMDs trilayer heterostructures as illustrated in Figure 2c. In the inset of Figure 2c, we observe two distinguishable modes at 243 cm⁻¹ (MoSe₂) and 247 cm⁻¹ (WSe₂). 20 nm-thick *h*-BN is used as an encapsulating layer due to its atomic smoothness and its relatively absence of charge traps and dangling bonds [60]. Raman shift of *h*-BN shows up in the TMDs-based trilayer heterostructure. The completed *h*-BN/WSe₂/MoSe₂/WSe₂ stacked structure is on a 290 nm SiO₂ substrate. To avoid undesired doping, we do not use any chemicals. With regards to the stacking geometry, we randomly stack our TMDs-based vdWs heterostructure since interlayer excitons can potentially be formed regardless of the layer orientation in vertically stacked heterostructures [8]. As shown in Figure 2d, PL spectroscopy is performed on our SL MoSe₂ and SL WSe₂ before and after transfer at varying temperatures, with the 1.88 eV pump excitation at ≈ 2 mW and with an ≈ 1 μ m beam spot size. PL spectra show each peak of the SL MoSe₂ (≈ 1.57 eV) and SL WSe₂ (≈ 1.64 eV) are obtained with high quantum efficiency; our trilayer shows two PL peaks captured by a Si detector. With decreasing temperature, both MoSe₂ and WSe₂ peaks are blue-shifted, consistent with prior studies [20,61-63]. The interlayer optical transition from the type-II heterojunction becomes dominant at low temperatures. As shown in the light brown line of Figure 2d, we observe that the PL intensities of the interlayer excitons can be larger even compared to those of intralayer excitons. (An example comparison of the trilayer to the bilayer is shown in Supplementary Section S3.) It is interesting to note that the addition of a WSe₂ layer to the MoSe₂-WSe₂ bilayer can result in higher PL quantum yields of both intralayer and interlayer excitons at room temperature and cryogenic temperatures.

Interlayer excitons in coupled quantum wells have previously been studied at low temperature in order to avoid thermal quenching of the PL due to nonradiative processes and electron-hole pairs excited to energies outside the light cone [29,30]. In Figure 3 we illustrate the temperature-dependent PL measurements from 4 K to 245 K of our trilayer atomic crystal, in order to examine the interlayer many-body excitonic transitions. Here we use a liquid-nitrogen-cooled InGaAs photodetector with high responsivity from 900 nm to 1600 nm. In our trilayer heterostructure, a long lower-energy spectral tail can be observed in the main interlayer exciton PL peak and becomes spectrally distinguishable from the neutral interlayer exciton (IEX₁) peak at 4 K as shown in Figure 3a (1.96 eV.pump excitation). We consequently deconvolved our trilayer interlayer lineshape into two peaks with Lorentzian lineshapes. The higher energy (black line fit) and lower energy (red line fit) peaks are denoted as IEX₁ and IEX₂ respectively, which we will subsequently attribute to the interlayer neutral excitons and trions (charged exciton) respectively as we will further elaborate below. The inset of Figure 3a shows the spectroscopy with our one-dimensional focal plane array InGaAs detector, with the horizontal axis the spectra and the vertical axis the spatial position across the sample via a scanning mirror.

Figure 3b shows the interlayer exciton spectra at different bath temperature, with the black (IEX₁) and red (IEX₂) lines tracking the spectral decomposition. It is worth noting that IEX₂ becomes distinguishable only at fairly low temperatures in the interlayer exciton lineshape. As shown in Figure 3b, both peaks are blue-shifted and broadened as the temperature increases and become undetectable above 245 K [20,61-63]. Figure 3c summarizes the measured temperature dependence of their peak positions, quantified by the band gap variation with temperature [64]. Linewidth temperature dependence and the phonon-induced bandgap renormalization model is described in Supplementary Sections S4 and S5 respectively. Under the same pump fluence and as shown in Figure 3c, we note that the energy difference between IEX₁ and IEX₂ does not change as temperature increases up to 126 K, the temperature after which the IEX₂ peak is too weak to distinguish with certainty. This is consistent with the fact that peak splitting of exciton and trion depends on the pumping fluence [16,65], further supported by our power-dependent PL spectra results later in this study.

Figure 3d and 3e show the neutral exciton and trion PL peak intensities and their ratio as a function of temperature. The PL peak intensities decrease with increasing temperature because in, for example, SL MoS₂ it is attributed to thermally excited excitons which escape the light cone [66]. Our reduced PL intensity with increasing temperature is attributed to the band structure of our trilayer heterostructure, which resembles that of SL MoSe₂ near the band edges

despite the existence of two WSe_2 layers. In addition we note that the phonon-assisted transitions move the weight from the main PL peak to lower energies and thereby reduce the PL peak intensities. Furthermore, since the promoted nonradiative process competes readily with radiative recombination of the interlayer excitons, the interlayer radiative recombination is not observed at room temperature. In Figure 3e we plot the ratio of PL peak intensities, $I_{\text{IEX}_2}/I_{\text{IEX}_1}$, which increases from ≈ 0.13 at 96 K to ≈ 0.28 at 4 K due to suppressed nonradiative recombination and high carrier densities. An abrupt rise around 10 K is typically induced by a rapidly increasing lifetime of trions and is a key feature of trions [20]. We note that the interlayer radiative recombination channels – in both the neutral exciton and trion – may involve the processes of optical phonons in order to conserve momentum in the band-to-band transition by optical phonon absorption and phonon emission. This is especially the case for the trion which has approximately two times larger FWHM than the neutral exciton (detailed in Supplementary Figure S4) and has a stronger thermal dependence.

In our experimental measurements we have assigned the two distinct interlayer PL emission peaks IEX_1 and IEX_2 to the neutral exciton and the three-body trion respectively. More details on the interlayer excitonic radiative recombination pathways are described in Supplementary Section 2 and Figure S2. For the lower energy (IEX_2) interlayer peak, we have also considered two other scenarios but both are unlikely. The first is a phonon-assisted indirect radiative recombination between valence band maximum (VBM) of WSe_2 at K-point and conduction band minimum (CBM) of MoSe_2 at Σ -point, per the band diagram of Figure 1c and 1d. However, based on our DFT calculations, the second valley at Σ -point of MoSe_2 CBM is located at ≈ 200 meV higher than K-point of MoSe_2 CBM. This large energy requirement makes it hard for the carriers to thermalize in this phonon-assisted transition, even at room temperature (≈ 25.7 meV). The second considered scenario is that of a potential sub-band above the K-point of MoSe_2 CBM. However, in our DFT calculations, we could not find the sub-band or energy splitting at MoSe_2 CBM nor the WSe_2 VBM. This further supports that the IEX_2 transition arises from the interlayer trions.

In Figure 4 we summarize the pump fluence dependence of the two interlayer excitons in our trilayer heterostructure by tuning the optical injection of the carriers. While the spectral shift of interlayer neutral exciton under increasing pump fluence has only a slight blue-shift, the spectral position of the trion is significantly more red-shifted with increasing pump fluence. This is illustrated in Figure 4a. Figure 4b summarizes the extracted energy difference between the peaks of the two electronic states for increasing photocarrier injection, illustrating a resulting linear dependence. A description of the two peak energy difference and the trion binding energy, in the

presence of carrier screening, is detailed in Supplementary Section S2. Based on this energy splitting, we extract the trion binding energy of ≈ 27 meV from Figure 4b [19], which is higher than the thermal activation energy at room temperature and even comparable with intralayer trion binding energy of SL TMDs [16,19-21,59,67]. This increasing spectral shift and binding energy with photocarrier density is another evidence for the interlayer trions [19,39]. This is because, with increasing photocarrier injection, free charge requires more energy to occupy the three-body trion excitonic states. In turn, we plot the PL spectral weights of the neutral exciton and trion in Figure 4c for increasing excitation fluence. With increasing photocarrier injection, the spectral weight and the ratio of the trion to the neutral exciton increases, which is supporting evidence of the interlayer trions existence [39].

We further investigate the lifetimes of the interlayer neutral exciton and trion, to help elucidate the many-body process. We build the TRPL setup by means of a time-correlated single-photon counting system (TCSPC) and conduct temperature-, pump fluence-, and pump wavelength-dependent TRPL experiments. All results are fitted biexponentially to the experimental data. Radiative recombination of excitons is difficult to obtain at room temperature because nonradiative recombination is dominant. Accordingly we perform lifetime measurements at cryogenic temperatures, with $\approx 9 \mu\text{J}/\text{cm}^2$ pump fluence and 1.88 eV (660 nm) pump wavelength, above both the SL MoSe₂ and SL WSe₂ direct gaps. Figure 5a and 5b summarizes the recombination lifetimes of interlayer neutral exciton and trion at various cryogenic temperatures. We note that, in the measurement of the IEX₂ lifetimes, we band-pass filter the spectrum with center wavelength around 990 ± 2 nm and FWHM of 10 ± 2 nm, to select the PL centered ≈ 985 nm in order to exclude the dynamics of the interlayer neutral exciton. As shown in Figure 5a, the lifetimes of our trilayer heterostructure interlayer exciton (IEX₁) are ≈ 2.54 ns (4 K), 2.47 ns (40 K), 1.84 ns (80 K), and 0.41 ns (120 K), on the same order-of-magnitude as prior bilayer heterostructure studies [53] and theoretical calculations [32]. For our trilayer heterostructure interlayer trion (IEX₂) they are ≈ 1.24 ns (4 K) and 0.47 ns (20 K). At higher bath temperatures, nonradiative recombination (including phonon-assisted processes) is faster, resulting in the shorter effective lifetimes observed.

Figure 5c summarizes the extracted lifetimes from Figure 5a and 5b. Although the data points are sparse, it seems that the interlayer trion (IEX₂) is more sensitive to the phonon processes than the interlayer neutral exciton (IEX₁) from the time-correlated single-photon counting measurements. This also correlates with the observed faster trion lifetimes in the finite bath temperature TRPL and the broader linewidths of the trions. We note that the lifetime of the

interlayer trion is not observable above 20 K due to the low photon counts. Meanwhile we note that the lifetime of interlayer exciton decreases linearly with increasing temperature.

To further explore the properties of interlayer exciton, we turn our attention to the interlayer exciton lifetimes under various pump fluences and pump wavelengths. As shown in Figure 5d and 5e, the lifetime of interlayer exciton (IEX_1) is weakly dependent on carrier injection compared to the bath temperature. As the pump fluence increases, the lifetime only decreases slightly from ≈ 2.72 ns ($1.6 \mu\text{J}/\text{cm}^2$) to ≈ 2.53 ns ($8.1 \mu\text{J}/\text{cm}^2$). With increasing pump fluence, the interlayer exciton density increases which causes a blue-shift. The dipolar exciton-exciton interaction may lead to the change of peak positions and the decrease of lifetime [68]. The decrease of lifetime with increasing excitation fluence indicates that residual defect states are involved, as shown in Figure 5d for the IEX_1 interlayer lifetime (lifetime of IEX_2 with increasing excitation fluence is not distinctly resolvable). The presence of residual defects also explains why the PL intensities of interlayer exciton and trion decrease as temperature increases. We also conduct pump wavelength-resolved TRPL experiment which is detailed in Supplementary Section S6. There is no correlation between the pump wavelength and the lifetimes of the interlayer exciton. This is because the electron-phonon decay dynamics to the band edge in TMDs is on the order of picoseconds, much shorter than the radiative recombination of interlayer excitons [69-71].

CONCLUSIONS

In this study we demonstrated the enhanced Coulomb interactions in $\text{WSe}_2\text{-MoSe}_2\text{-WSe}_2$ trilayer vdWs heterostructures, through interlayer radiative recombination of the neutral and charge excitonic states. Designed through spin-polarized density functional theory with exchange correlation and spin-orbit coupling, we examined type-II heterostructures with increased optical transition oscillator strengths. Fabricated via *h*-BN enabled dry transfer, the trilayer heterostructure exhibits an $\approx 3\times$ (at 77 K) and $5\times$ (at lower temperature) stronger photoluminescence in our measurements. This arises from the more spatially distributed hybridized valence band state across the trilayer which, while the conduction band is localized only at the MoSe_2 layer, enables larger overlap and oscillator strengths. Our cryogenic steady-state and time-resolved photoluminescence measurements elucidate the additional presence of a three-body excitonic state in the interlayer radiative recombination, with the trion binding at ≈ 27 meV and largely dependent on the pump fluence and carrier densities instead of the bath temperature. Conversely the trilayer interlayer radiative lifetimes are largely dependent on the bath temperature instead of the pump fluence and exciton wavelengths, promoted by

phonon-assisted transitions. The relatively long radiative lifetimes measured up to 2.54 ns at 4 K enables next-generation excitonic devices [72]. Future experiments include gating the heterostructures with controlled carrier densities and spectrally separated excitonic resonances to further clarify their roles in exciton dephasing and population relaxation [17, 73]. With advanced 2D material growth techniques and computational methods [27,74], we believe our trilayer heterostructures support the understanding of interlayer light-matter interactions with facilitated carrier transfer and type-II heterojunctions, paving new ways to tailor the electronic and optoelectronic character of vdWs heterostructures.

REFERENCES

1. Amani, M., Lien, D.-H., Kiriya, D., Xiao, J., Azcatl, a., Noh, J., Madhvapathy, S. R., Addou, R., Kc, S., Dubey, M., Cho, K., Wallace, R. M., Lee, S.-C., He, J.-H., Ager, J. W., Zhang, X., Yablonovitch, E., Javey, A. Near-unity photoluminescence quantum yield in MoS₂. *Science* 2015; **350**: 1065–1068.
2. Lin, Y., Ling, X., Yu, L., Huang, S., Hsu, A. L., Lee, Y. H., Kong, J., Dresselhaus, M. S., Palacios, T. Dielectric screening of excitons and trions in single-layer MoS₂. *Nano Letters* 2014; **14**: 5569–5576.
3. Kato, Y. K., Myers, R. C., Gossard, A. C., Awschalom, D. D. Observation of the spin hall effect in semiconductors. *Science* 2004; **306**: 1910–1913.
4. Xiaodong, Xu. Wang, Yao. Di, Xiao. Heinz, T. F. Spin and pseudospins in layered transition metal dichalcogenides. *Nature Physics* 2014; **10**: 343–350.
5. Mak, K. F., He, K., Shan, J., Heinz, T. F. Control of valley polarization in monolayer MoS₂ by optical helicity. *Nature Nanotechnology* 2012; **7**: 494–498.
6. Wang, H., Yu, L., Lee, Y. H., Shi, Y., Hsu, A., Chin, M. L., Li, L. J., Dubey, M., Kong, J., Palacios, T. Integrated circuits based on bilayer MoS₂ transistors. *Nano Letters* 2012; **12**: 4674–4680.
7. Low, T., Chaves, A., Caldwell, J. D., Kumar, A., Fang, N. X., Avouris, P., Heinz, T. F., Guinea, F., Martin-Moreno, L., Koppens, F. Polaritons in layered 2D materials. *Nature Materials* 2016; **16**: 182–194.
8. Chen, H., Wen, X., Zhang, J., Wu, T., Gong, Y., Zhang, X., Yuan, J., Yi, C., Lou, J., Ajayan, P. M., Zhuang, W., Zhang, G., Zheng, J. Ultrafast formation of interlayer hot excitons in atomically thin MoS₂/WS₂ heterostructures. *Nature Communications* 2016; **7**: 12512.

9. Zhu, W., Low, T., Lee, Y. H., Wang, H., Farmer, D. B., Kong, J., Xia, F., Avouris, P. Electronic transport and device prospects of monolayer molybdenum disulphide grown by chemical vapour deposition. *Nature Communications* 2014; **5**: 3087.
10. Sim, S., Lee, D., Noh, M., Cha, S., Soh, C. H., Sung, J. H., Jo, M.-H., Choi, H. Selectively tunable optical Stark effect of anisotropic excitons in atomically thin ReS₂. *Nature Communications* 2016; **7**: 13569.
11. Cha, S., Sung, J. H., Sim, S., Park, J., Heo, H., Jo, M.-H., Choi, H. 1s-intraexcitonic dynamics in monolayer MoS₂ probed by ultrafast mid-infrared spectroscopy. *Nature Communications* 2016; **7**: 10768.
12. Radisavljevic, B., Radenovic, A., Brivio, J., Giacometti, V., Kis, A. Single-layer MoS₂ transistors. *Nature Nanotechnology* 2011; **6**: 147–150.
13. Wang, Q. H., Kalantar-Zadeh, K., Kis, A., Coleman, J. N., Strano, M. S. Electronics and optoelectronics of two-dimensional transition metal dichalcogenides. *Nature Nanotechnology* 2012; **7**: 699–712.
14. Yuan, L., Huang, L. Exciton dynamics and annihilation in WS₂ 2D semiconductors. *Nanoscale* 2015; **7**: 7402–7408.
15. He, K., Kumar, N., Zhao, L., Wang, Z., Mak, K. F., Zhao, H., Shan, J. Tightly bound excitons in monolayer WSe₂. *Physical Review Letters* 2014; **113**: 026803.
16. Mak, K. F., He, K., Lee, C., Lee, G. H., Hone, J., Heinz, T. F., Shan, J. Tightly bound trions in monolayer MoS₂. *Nature Materials* 2013; **12**: 207–211.
17. Sie, E. J., Lee, C.H., Lee, Y.-H., Fu, L., Kong, J., Gedik, N. Large, valley-exclusive Bloch-Siegert shift in monolayer WS₂. *Science* 2017; **355**: 1066-1069.
18. Jones, A. M., Yu, H., Schaibley, J. R., Yan, J., Mandrus, D. G., Taniguchi, T., Watanabe, K., Dery, H., Yao, W., Xu, X. Excitonic luminescence upconversion in a two-dimensional semiconductor. *Nature Physics* 2015; **12**: 323–327.
19. Jones, A. M., Yu, H., Ghimire, N. J., Wu, S., Aivazian, G., Ross, J. S., Zhao, B., Yan, J., Mandrus, D. G., Xiao, D., Yao, W., Xu, X. Optical generation of excitonic valley coherence in monolayer WSe₂. *Nature Nanotechnology* 2013; **8**: 634–638.
20. Ross, J. S., Wu, S., Yu, H., Ghimire, N. J., Jones, A. M., Aivazian, G., Yan, J., Mandrus, D. G., Xiao, D., Yao, W., Xu, X. Electrical control of neutral and charged excitons in a monolayer semiconductor. *Nature Communications* 2013; **4**: 1474.

21. Aivazian, G., Gong, Z., Jones, a M., Chu, R. L., Yan, J., Mandrus, D. G., Zhang, C., Cobden, D., Yao, W., Xu, X. D. Magnetic control of valley pseudospin in monolayer WSe₂. *Nature Physics* 2014; **11**: 148–152.
22. You, Y., Zhang, X.-X., Berkelbach, T. C., Hybertsen, M. S., Reichman, D. R., Heinz, T. F. Observation of biexcitons in monolayer WSe₂. *Nature Physics* 2015; **11**: 477–481.
23. Kim, J., Park, H., Hannon, J. B., Bedell, S. W., Fogel, K., Sadana, D. K., Dimitrakopoulos, C. Layer-resolved graphene transfer via engineered strain layers. *Science* 2013; **342**: 833–836.
24. Bae, S.-H., Zhou, X., Kim, S., Lee, Y. S., Cruz, S. S., Kim, Y., Hannon, J. B., Yang, Y., Sadana, D. K., Ross, F. M., Park, H., Kim, J. Unveiling the carrier transport mechanism in epitaxial graphene for forming wafer-scale, single-domain graphene. *Proceedings of the National Academy of Sciences* 2017; **114**: 4082–4086.
25. Liu, Y., Wu, H., Cheng, H. C., Yang, S., Zhu, E., He, Q., Ding, M., Li, D., Guo, J., Weiss, N. O., Huang, Y., Duan, X. Toward barrier free contact to molybdenum disulfide using graphene electrodes. *Nano Letters* 2015; **15**: 3030–3034.
26. Cheng, H. C., Wang, G., Li, D., He, Q., Yin, A., Liu, Y., Wu, H., Ding, M., Huang, Y., Duan, X. Van der Waals heterojunction devices based on organohalide perovskites and two-dimensional materials. *Nano Letters* 2016; **16**: 367–373.
27. Li, M.-Y., Shi, Y., Cheng, C.-C., Lu, L.-S., Lin, Y.-C., Tang, H.-L., Tsai, M.-L., Chu, C.-W., Wei, K.-H., He, J.-H., Chang, W.-H., Suenaga, K., Li, L.-J. Epitaxial growth of a monolayer WSe₂-MoS₂ lateral *p-n* junction with an atomically sharp interface. *Science* 2015; **349**: 524–528.
28. Kim, Y., Cruz, S. S., Lee, K., Alawode, B. O., Choi, C., Song, Y., Johnson, J. M., Heidelberger, C., Kong, W., Choi, S., Qiao, K., Almansouri, I., Fitzgerald, E. A., Kong, J., Kolpak, A. M., Hwang, J., Kim, J. Remote epitaxy through graphene enables two dimensional material-based layer transfer. *Nature* 2017; **544**: 340–343.
29. Butov, L. V., Zrenner, A., Abstreiter, G., Bohm, G., Weimann, G. Condensation of indirect excitons in coupled AlAs /GaAs quantum wells. *Physical Review Letters* 1994; **73**: 304-307.
30. Butov, L., Imamoglu, A., Mintsev, A., Campman, K., Gossard, A. Photoluminescence kinetics of indirect excitons in GaAs/Al_xGa_{1-x}As coupled quantum wells. *Physical Review B* 1999; **59**: 1625–1628.
31. Rivera, P., Seyler, K. L., Yu, H., Schaibley, J. R., Yan, J., Mandrus, D. G. Yao, W. Xu, X.

- Valley-polarized exciton dynamics in a 2D semiconductor heterostructure. *Science* 2016; **35**: 668–690.
32. Rivera, P., Schaibley, J. R., Jones, A. M., Ross, J. S., Wu, S., Aivazian, G., Klement, P., Seyler, K., Clark, G., Ghimire, N. J., Yan, J., Mandrus, D. G., Yao, W., Xu, X. Observation of long-lived interlayer excitons in monolayer MoSe₂–WSe₂ heterostructures. *Nature Communications* 2015; **6**: 6242.
 33. Jones, A. M., Yu, H., Ross, J. S., Klement, P., Ghimire, N. J., Yan, J., Mandrus, D. G., Yao, W., Xu, X. Spin–layer locking effects in optical orientation of exciton spin in bilayer WSe₂. *Nature Physics* 2014; **10**: 130–134.
 34. Gong, C., Zhang, H., Wang, W., Colombo, L., Wallace, R. M., Cho, K. Band alignment of two-dimensional transition metal dichalcogenides: Application in tunnel field effect transistors. *Applied Physics Letters* 2013; **103**: 053513.
 35. Özçelik, V. O., Azadani, J. G., Yang, C., Koester, S. J., Low, T. Band alignment of two dimensional semiconductors for designing heterostructures with momentum space matching. *Physical Review B* 2016; **94**: 035125.
 36. Mak, K. F., Shan, J. Photonics and optoelectronics of 2D semiconductor transition metal dichalcogenides. *Nature Photonics* 2016; **10**: 216–226.
 37. Palummo, M., Bernardi, M., Grossman, J. C. Exciton radiative lifetimes in two dimensional transition metal dichalcogenides. *Nano Letters* 2015; **15**: 2794–2800.
 38. Chiu, M.-H., Zhang, C., Shiu, H.-W., Chuu, C.-P., Chen, C.-H., Chang, C.-Y. S., Chen, C.-H., Chou, M.-Y., Shih, C.-K., Li, L.-J. Determination of band alignment in the single layer MoS₂/WSe₂ heterojunction. *Nature Communications* 2015; **6**: 7666.
 39. Bellus, M. Z., Ceballos, F., Chiu, H., Zhao, H. Tightly bound trions in transition metal dichalcogenide heterostructures. *ACS Nano* 2015; **9**: 6459–6464.
 40. Chiu, M. H., Li, M. Y., Zhang, W., Hsu, W. T., Chang, W. H., Terrones, M., Terrones, H., Li, L. J. Spectroscopic signatures for interlayer coupling in MoS₂-WSe₂ van der Waals stacking. *ACS Nano* 2014; **8**: 9649–9656.
 41. Zhang, J., Wang, J. H., Chen, P., Sun, Y., Wu, S., Jia, Z. Y., Lu, X. B., Yu, H., Chen, W., Zhu, J. Q., Xie, G. B., Yang, R., Shi, D. X., Xu, X. L., Xiang, J. Y., Liu, K. H., Zhang, G. Y. Observation of strong interlayer coupling in MoS₂/WS₂ heterostructures. *Advanced Materials* 2016; **28**: 1950–1956.

42. Hill, H. M., Rigosi, A. F., Rim, K. T., Flynn, G. W., Heinz, T. F. Band alignment in MoS₂/WS₂ transition metal dichalcogenide heterostructures probed by scanning tunneling microscopy and spectroscopy. *Nano Letters* 2016; **16**: 4831–4837.
43. Leu, P. W., Shan, B., Cho, K. Surface chemical control of the electronic structure of silicon nanowires: density functional calculations. *Physical Review B* 2006; **73**: 195320.
44. Tongay, S., Zhou, J., Ataca, C., Lo, K., Matthews, T. S., Li, J., Grossman, J. C., Wu, J. Thermally driven crossover from indirect toward direct bandgap in 2D semiconductors: MoSe₂ versus MoS₂. *Nano Letters* 2012; **12**: 5576–5580.
45. Cai, Y., Zhang, G., Zhang, Y.-W. Layer-dependent band alignment and work function of few-layer phosphorene. *Scientific reports* 2014; **4**: 6677.
46. Yan, J.-A., Yang, L., Chou, M. Y. Size and orientation dependence in the electronic properties of silicon nanowires. *Physical Review B* 2007; **76**: 115319.
47. Lin, L., Li, Z., Feng, J., Zhang, Z. Indirect to direct band gap transition in ultra-thin silicon films. *Physical chemistry chemical physics : PCCP* 2013; **15**: 6063–6067.
48. Grimmer, S. Semiempirical GGA-type density functional constructed with a long-range dispersion correction. *Journal of Computational Chemistry* 2006; **27**: 1787–1799.
49. Blöchl, P. E. Projector augmented-wave method. *Physical Review B* 1994; **50**: 17953.
50. Perdew, J. P., Burke, K., Ernzerhof, M. Generalized gradient approximation made simple. *Physical Review Letters* 1996; **77**: 3865-3868.
51. Kresse, G., Furthmüller, J. Efficient iterative schemes for ab initio total-energy calculations using a plane-wave basis set. *Physical Review B* 1996; **54**: 11169.
52. Feenstra, R. M., Srivastava, N., Gao, Q., Widom, M., Diaconescu, B., Ohta, T., Hellogg, G. L., Robinson, J. T., Vlassiuk, I. V. Low-energy electron reflectivity from graphene. *Physical Review B* 2013; **87**: 041406.
53. Rigosi, A. F., Hill, H. M., Li, Y., Chernikov, A., Heinz, T. F. Probing interlayer interactions in transition metal dichalcogenide heterostructures by optical spectroscopy: MoS₂/WS₂ and MoSe₂/WSe₂. *Nano Letters* 2015; **15**: 5033–5038.
54. Hong, X., Kim, J., Shi, S.-F., Zhang, Y., Jin, C., Sun, Y., Tongay, S., Wu, J., Zhang, Y., Wang, F. Ultrafast charge transfer in atomically thin MoS₂/WS₂ heterostructures. *Nature Nanotechnology* 2014; **9**: 682-686.

55. Kozawa, D., Carvalho, A., Verzhbitskiy, I., Giustiniano, F., Miyauchi, Y., Mouri, S., Castro Neto, A. H., Matsuda, K., Eda, G. Evidence for fast interlayer energy transfer in MoSe₂/WS₂ heterostructures. *Nano Letters* 2016; **16**: 4087–4093.
56. Wang, Y., Wang, Z., Yao, W., Liu, G. B., Yu, H. Interlayer coupling in commensurate and incommensurate bilayer structures of transition-metal dichalcogenides. *Physical Review B* 2017; **95**: 115429.
57. Kim, J., Jin, C., Chen, B., Cai, H., Zhao, T., Lee, P., Kahn, S., Watanabe, K., Taniguchi, T., Tongay, S., Crommie, M. F., Wang, F. Observation of ultralong valley lifetime in WSe₂/MoS₂ heterostructures. *Science Advances* 2016; **3**: e1700518.
58. Robert, C., Lagarde, D., Cadiz, F., Wang, G., Lassagne, B., Amand, T., Balocchi, A., Renucci, P., Tongay, S., Urbaszek, B., Marie, X. Exciton radiative lifetime in transition metal dichalcogenide monolayers. *Physical Review B* 2016; **93**: 205423.
59. Singh, A., Moody, G., Tran, K., Scott, M. E., Overbeck, V., Berghauser, G., Schaibley, J., Seifert, E. J., Pleskot, D., Gabor, N. M., Yan, J., Mandrus, D. G., Richter, M., Malic, E., Xu, X., Li, X. Trion formation dynamics in monolayer transition metal dichalcogenides. *Physical Review B* 2016; **93**: 041401.
60. Dean, C. R., Young, a F., Meric, I., Lee, C., Wang, L., Sorgenfrei, S., Watanabe, K., Taniguchi, T., Kim, P., Shepard, K. L., Hone, J. Boron nitride substrates for high-quality graphene electronics. *Nature Nanotechnology* 2010; **5**: 722–726.
61. Wang, G., Bouet, L., Lagarde, D., Vidal, M., Balocchi, A., Amand, T., Marie, X., Urbaszek, B. Valley dynamics probed through charged and neutral exciton emission in monolayer WSe₂. *Physical Review B* 2014; **90**: 075413.
62. Molina-Sánchez, A., Palumbo, M., Marini, A., Wirtz, L. Temperature-dependent excitonic effects in the optical properties of single-layer MoS₂. *Physical Review B* 2016; **93**: 155435.
63. Zhang, S., Wang, C. G., Li, M. Y., Huang, D., Li, L. J., Ji, W., Wu, S. Defect structure of localized excitons in a WSe₂ monolayer. *Physical Review Letters* 2017; **119**: 046101.
64. O'Donnell, K. P., Chen, X. Temperature dependence of semiconductor band gaps. *Applied Physics Letters* 1991; **58**: 2924–2926.
65. Zhang, C., Wang, H., Chan, W., Manolatos, C., Rana, F. Absorption of light by excitons and trions in monolayers of metal dichalcogenide MoS₂: Experiments and theory. *Physical Review B* 2014; **89**: 205436.

66. Withers, F., Del Pozo-Zamudio, O., Schwarz, S., Dufferwiel S, Walker, P. M., Godde, T., Rooney, A. P., Gholinia, A., Woods, C. R., Blake, P., Haigh, S. J., Watanabe, K., Taniguchi, T., Aleiner, I. L., Geim, A. K., Fal'ko, V. I., Tartakovskii, A. I., Novoselov, K. S. WSe₂ light-emitting tunneling transistors with enhanced brightness at room temperature. *Nano Letters* 2015; **15**: 8223–8228.
67. Berkelbach, T. C., Hybertsen, M. S., Reichman, D. R. Theory of neutral and charged excitons in monolayer transition metal dichalcogenides. *Physical Review B* 2013; **88**: 045318.
68. Nagler, P., Plechinger, G., Ballottin, M. V., Mitioglu, A., Meier, S., Paradiso, N., Strunk, C., Chernikov, A., Christianen, P. C. M., Schüller, C., Korn, T. Interlayer exciton dynamics in a dichalcogenide monolayer heterostructure. *2D Materials* 2017; **4**: 025112.
69. Wang, H., Zhang, C., Rana, F. Ultrafast dynamics of defect-assisted electron-hole recombination in monolayer MoS₂. *Nano Letters* 2015; **15**: 339–345.
70. Lui, C. H., Ye, Z., Ji, C., Chiu, K. C., Chou, C. T., Andersen, T. I., Means-Shively, C., Anderson, H., Wu, J. M., Kidd, T., Lee, Y. H., He, R. Observation of interlayer phonon modes in van der Waals heterostructures. *Physical Review B* 2015; **91**: 165403.
71. Yu, Y., Hu, S., Su, L., Huang, L., Liu, Y., Jin, Z., Alexander, A., Geohegan, D. B., Kim, K. W., Zhang, Y., Cao, L. Equally efficient interlayer exciton relaxation and improved absorption in epitaxial and nonepitaxial MoS₂/WS₂ heterostructures. *Nano Letters* 2015; **15**: 486–491.
72. Grosso, G., Graves, J. C., Hammack, A. T., High, A. a., Butov, L. V., Hanson, M., Gossard, A. C. Excitonic switches operating at around 100 K. *Nature Photonics* 2010; **3**: 577–580.
73. Kim, J., Son, H., Cho, D. J., Geng, B. S., Regan, W., Shi, S. F., Kim, K., Zettl, A, Shen, Y. R., Wang, F. Electrical control of optical plasmon resonance with graphene. *Nano Letters* 2012; **12**: 5598–5602.
74. Latini, S., Winther, K. T., Olsen, T., Thygesen, K. S. Interlayer excitons and band alignment in MoS₂/hBN/WSe₂ van der Waals heterostructures. *Nano Letters* 2017; **17**: 938–945.

Author contributions: C.C. designed this work. C.C. and H.K. performed the optical measurements and data analysis. H.-C.C. and C.C. led the device fabrication. C.C., J.C and S.B. provided TMDs materials and sample characterizations. C.C., A.V., S.-W.H., V.O.Ö., R.G., K.K., T.L and C.W.W. contributed the theoretical analysis and simulations. C.W.W. supported and supervised the research. C.C., K.K., T.L. and C.W.W. prepared the manuscript.

Funding sources: We acknowledge support from the University of California – National Laboratory research program and the National Science Foundation (DMR-1611598).

Financial interest: The authors declare no competing financial interest.

Acknowledgements: The authors are grateful for helpful discussions with Philip Kim, Tony van Buuren, Baicheng Yao, Jinkang Lim, Jiahui Huang, Yandong Luo, Jin Ho Kang.

Supplementary Information: Supplementary Information for this article can be found online.

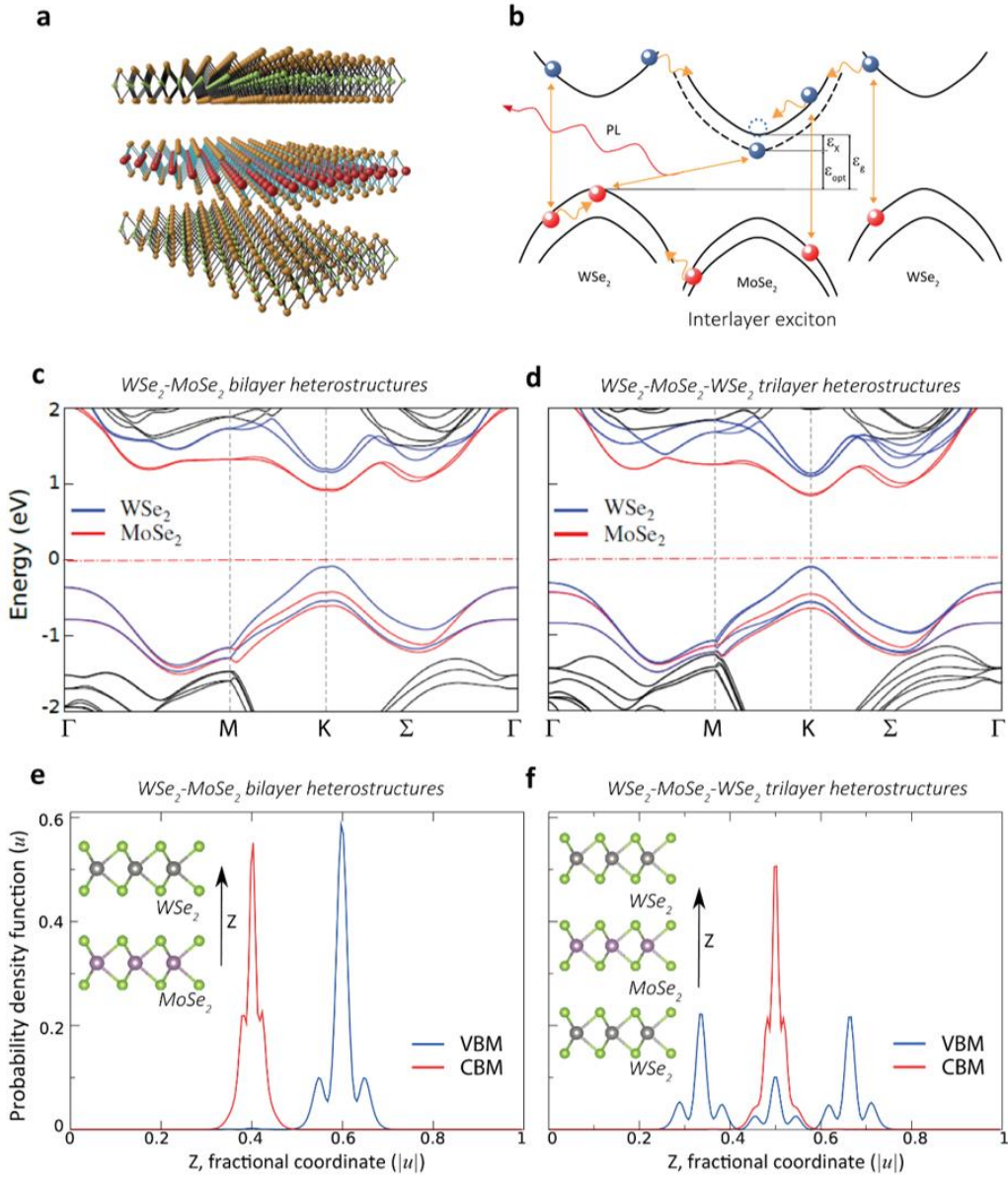


Figure 1 | Excitonic states of TMDs-based trilayer heterostructure, interlayer excitons model, and computed band structure and wavefunction distribution comparisons between the bilayer and trilayer heterostructures. **a**, Illustration of $\text{WSe}_2\text{-MoSe}_2\text{-WSe}_2$ trilayer heterostructure with a sandwiched single layer (SL) MoSe_2 between two SLs WSe_2 . **b**, Schematic summary of the interlayer exciton radiative recombination predicted by type-II heterojunction. ϵ_X , ϵ_{opt} and ϵ_g represent the exciton binding energy, optical gap and electronic gap respectively. **c**, Computed band structure of the $\text{WSe}_2\text{-MoSe}_2$ bilayer heterostructure. **d**, Computed band structure of the $\text{WSe}_2\text{-MoSe}_2\text{-WSe}_2$ trilayer heterostructure. **e**, Computed orbital wavefunction of the $\text{WSe}_2\text{-MoSe}_2$ bilayer heterostructure valence band maximum (VBM) and conduction band minimum (CBM) at k -point as a function of the interlayer distance z . **f**, Computed orbital wavefunction of the $\text{WSe}_2\text{-MoSe}_2\text{-WSe}_2$ trilayer heterostructure.

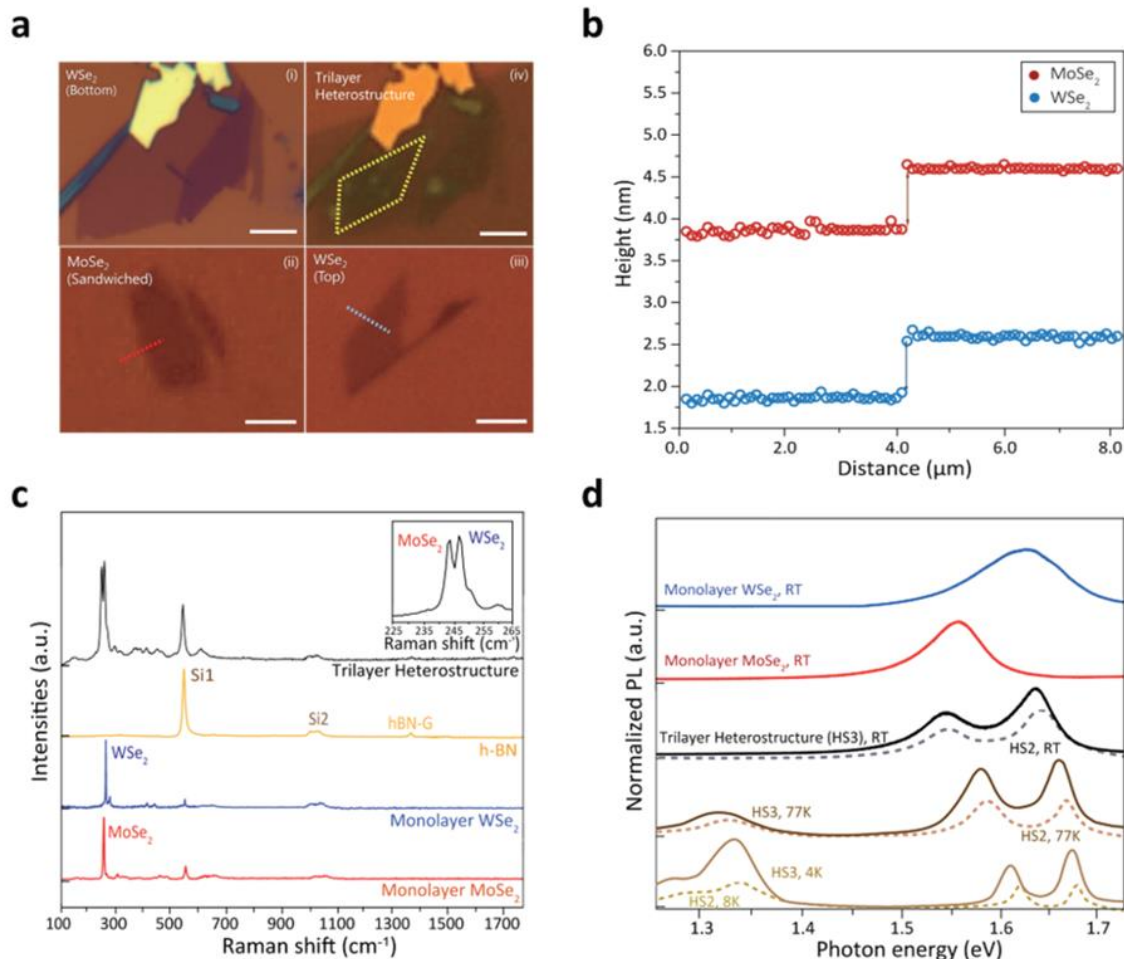


Figure 2 | TMDs-based trilayer van der Waals (vdWs) heterostructure fabrication and characterization. **a**, Microscopic images of the exfoliated transition metal dichalcogenides monolayers [i – iii] and trilayer vdWs heterostructure [iv] on SiO_2 substrate. The dashed red and blue lines in the lower panels denote the atomic force microscopy (AFM) regions. The area enclosed by dashed yellow line indicates the trilayer heterostructure region. Scale bar: $5 \mu\text{m}$. **b**, AFM cross-sectional profiles, where each atomic single-layer (SL) is $\approx 7 \text{ \AA}$. WSe_2 and MoSe_2 are the blue and red lines respectively. **c**, Raman spectra of the trilayer heterostructure versus each SL (MoSe_2 , WSe_2 , $h\text{-BN}$) decomposition, pumped with a 532 nm laser. Inset: zoom-in of the Raman shift around 245 cm^{-1} . **d**, Room-temperature PL spectra for the SL WSe_2 , SL MoSe_2 and the trilayer heterostructure, together with the low-temperature PL spectra from the trilayer heterostructure at 77 K and 4 K. The excitation is via a 632 nm HeNe laser. Dotted lines under the trilayer heterostructure PL spectra are the bilayer heterostructure PL spectra, with especially large enhancement of the lower-energy interlayer exciton transition.

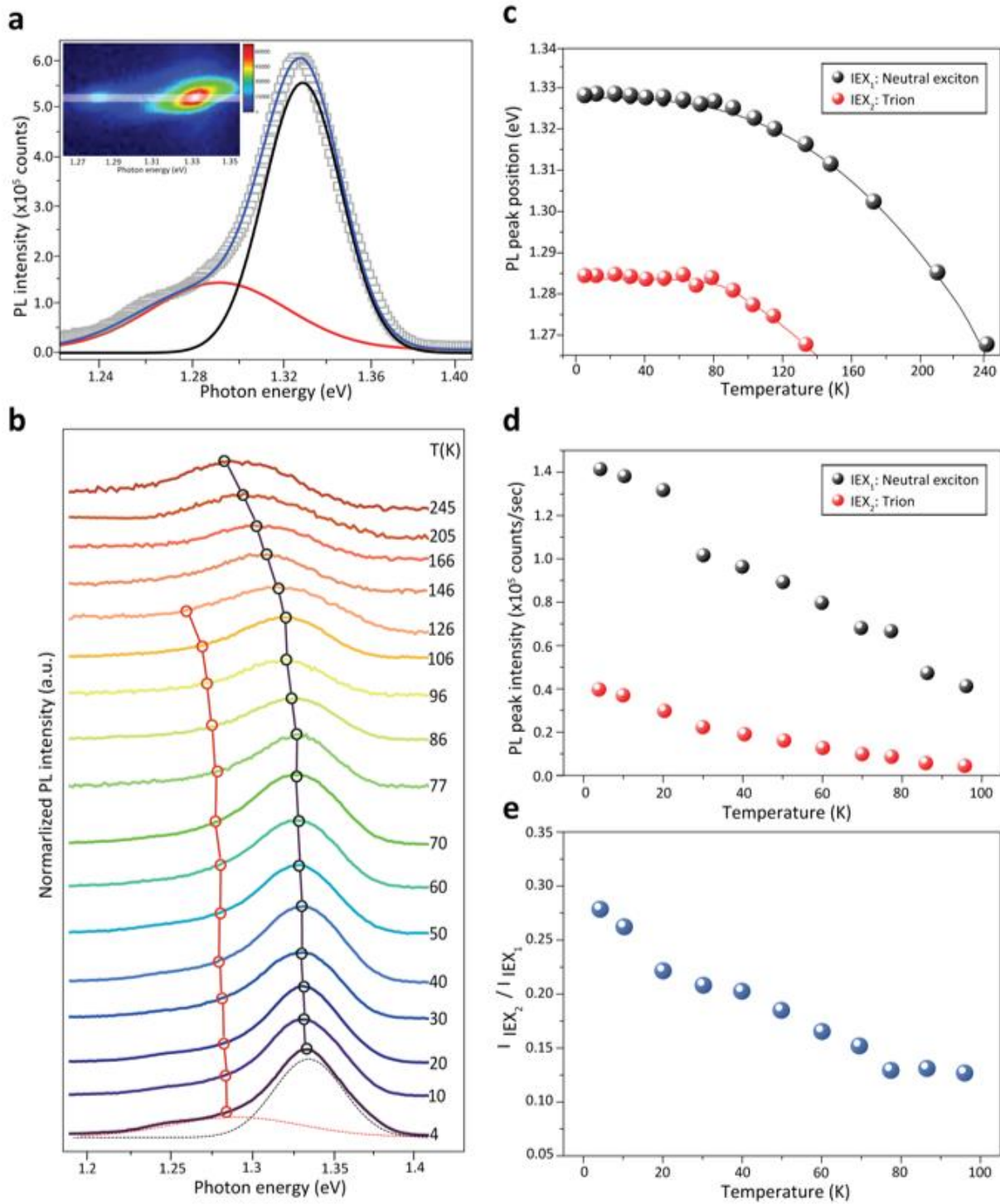


Figure 3 | Temperature-dependent PL intensities and spectral lineshapes of the interlayer excitons in the trilayer heterostructure. **a**, Indirect excitons PL spectra at 4 K, fitted with a blue line. Both IEX₁: neutral exciton (black) and IEX₂: trion (red) lines are fitted with Lorentzian lineshapes. Inset image shows PL spectrum captured by a focal plane array detector with horizontal axis the spectra and the vertical axis the spatial position across the sample in one

direction. **b**, Temperature-dependent indirect PL spectra in trilayer heterostructure with pump excitation at 1.96 eV and ≈ 1.2 mW reaching sample. The black and red lines denoted the respective peaks, with the dashed black and red curves at the 4K spectra illustrating the Lorentzian lineshape decomposition. The data were obtained from the same spot on the sample. The spectra are offset for clarity. **c**, PL peak shifts of the neutral exciton (IEX_1) and trion (IEX_2) deduced from the main panel and fitted with semiconductor bandgap temperature-dependence model. The phonon-induced bandgap renormalization is described in Supplementary Section S5. **d**, PL peak intensities at different cryogenic temperatures. Black and red dots indicate the PL intensities of neutral exciton and trion respectively. **e**, The ratio of neutral exciton (IEX_1) to trion (IEX_2) peak intensities in the trilayer heterostructure are illustrated as a function of bath temperature.

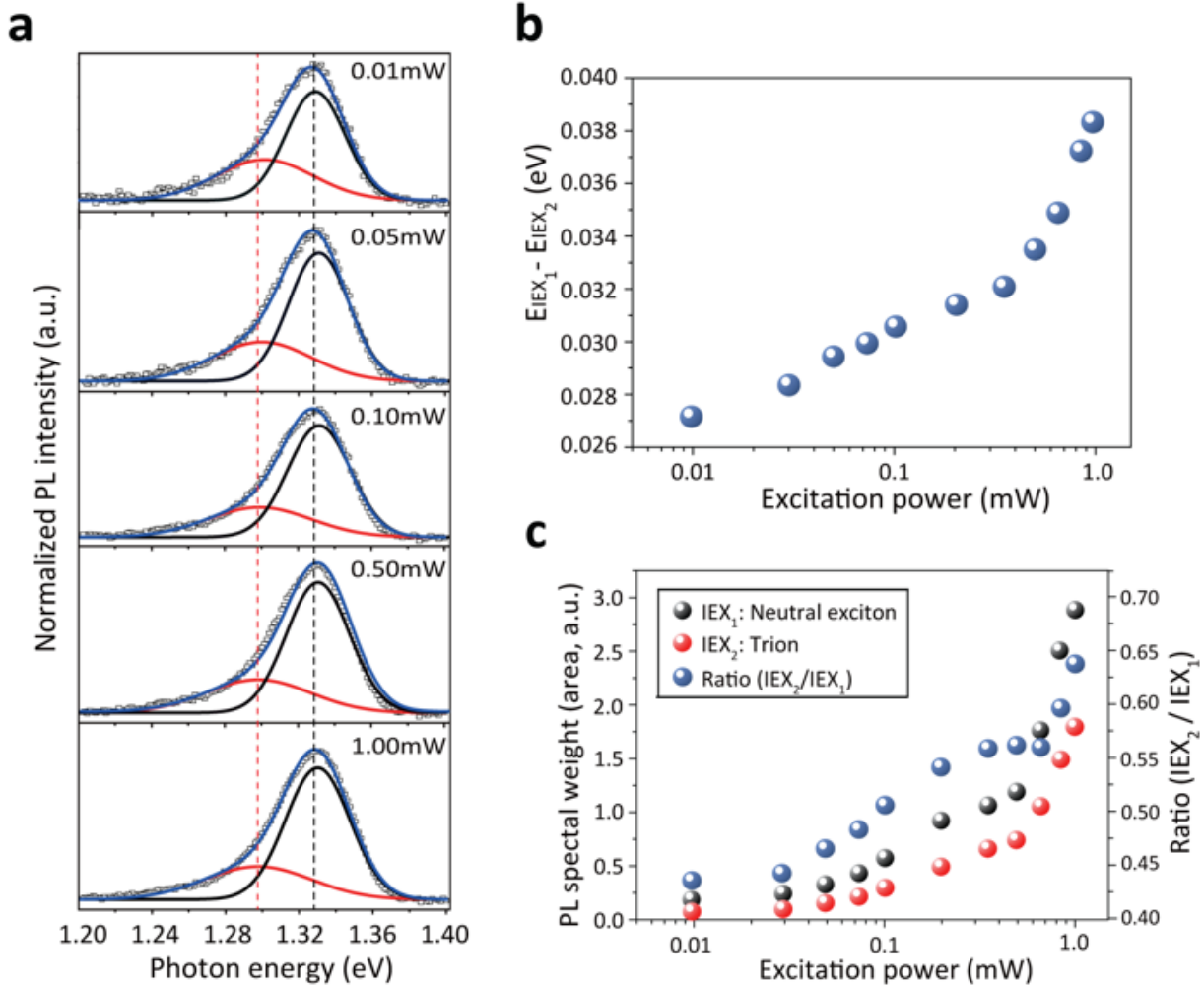


Figure 4 | Power-dependent PL spectra in the trilayer heterostructure at 4 K. **a**, Power-dependent PL spectra with Lorentzian-fitted neutral exciton (black curve) and trion (red curve) at 4 K. **b**, Energy splitting (trion binding energy: $E_{IEX_1} - E_{IEX_2}$) between two interlayer optical transition peaks as a function of excitation power (log scale). **c**, PL spectral weight of neutral exciton (black dots) and trion (red dots), and the ratio of trion to neutral exciton (blue dots), as a function of pump excitation power.

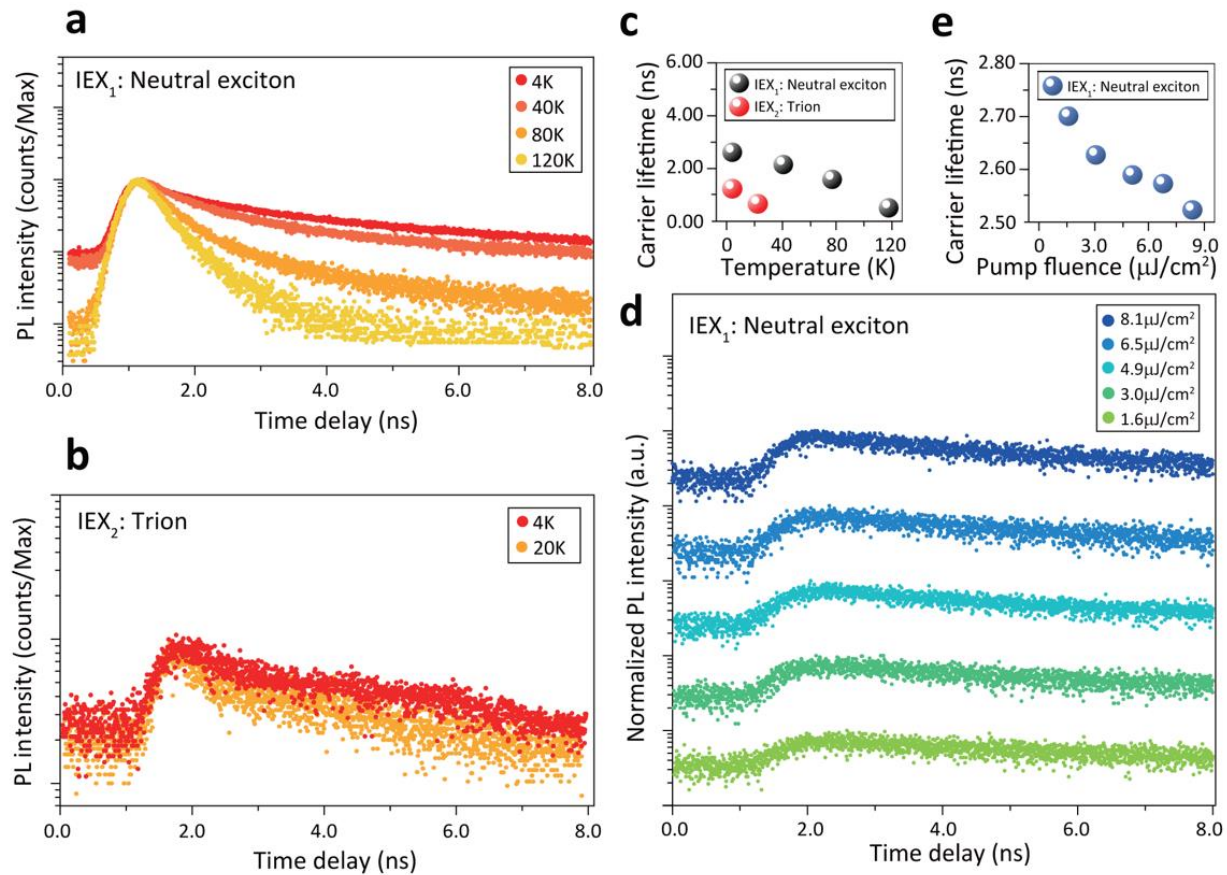


Figure 5 | Interlayer excitons lifetime and its dependence on temperature and photocarrier injection in the trilayer heterostructure. **a** and **b**, Temperature-dependent carrier lifetimes of interlayer neutral exciton (IEX_1) and trion (IEX_2) in trilayer heterostructure. Samples are excited with $\approx 9 \mu\text{J}/\text{cm}^2$ power fluence at 1.88 eV (660 nm). **c**, Carrier lifetimes of IEX_1 and IEX_2 with different temperatures at pump fluence of $\approx 9 \mu\text{J}/\text{cm}^2$. The carrier relaxations are fitted with exponentials to extract the carrier lifetimes. **d**, Time-resolved radiative recombination of IEX_1 under different pump fluences at 4 K. **e**, Carrier lifetimes of IEX_1 under different pump fluences at 4 K.

Supplementary Information

Enhanced interlayer neutral excitons and trions in trilayer van der Waals heterostructures

Chanyeol Choi^{1,2,†}, Hung-Chieh Cheng^{3,4}, Hyunseok Kim², Abhinav Kumar Vinod^{1,2}, Sang-Hoon Bae^{3,4}, V. Ongun Özçelik⁵, Roberto Grassi⁶, Jongjae Chae³, Shu-Wei Huang^{1,2}, Xiangfeng Duan^{4,7}, Kristen Kaasbjerg⁸, Tony Low⁶, and Chee Wei Wong^{1,2,†}

¹ Fang Lu Mesoscopic Optics and Quantum Electronics Laboratory, University of California, Los Angeles, CA 90095, United States

² Department of Electrical Engineering, University of California, Los Angeles, CA 90095, United States

³ Department of Materials Science and Engineering, University of California, Los Angeles, CA 90095, United States

⁴ California Nanosystems Institute, University of California, Los Angeles, CA 90095, United States

⁵ Andlinger Center for Energy and the Environment, Princeton University, Princeton, New Jersey 08544, United States

⁶ Department of Electrical and Computer Engineering, University of Minnesota, Minneapolis, MN 55455, United States

⁷ Department of Chemistry and Biochemistry, University of California, Los Angeles, CA 90095, United States

⁸ Center for Nanostructured Graphene (CNG), Department of Micro- and Nanotechnology (DTU Nanotech), Technical University of Denmark, DK-2800 Kgs. Lyngby, Denmark

† Corresponding Authors: cowellchoi@gmail.com ; cheewei.wong@ucla.edu

Content

- S1. Computed band structures of single-layer (SL) MoSe₂ and WSe₂
- S2. Two interlayer excitons radiative recombination pathways
- S3. Integrated photoluminescence (PL) intensity in bilayer and trilayer heterostructures
- S4. Full width half maximum (FWHM) of two interlayer excitonic states
- S5. Semiconductor bandgap renormalization with temperature
- S6. Time-resolved photoluminescence (TRPL) with different excitation wavelengths

S1. Computed band structures of single-layer (SL) MoSe₂ and WSe₂

Figure 1 shows the results of computed band structures for SL MoSe₂ and WSe₂, based on the spin-polarized density functional theory (DFT) within the generalized gradient approximation (GGA) using the same set of parameters as presented in the main text. Both of these SL structures have D_{3h} group symmetry without inversion symmetry and have a direct band gap at the K point. The lattice constants of both MoSe₂ and WSe₂ SL structures are calculated as 3.33 Å with a nearest neighbor Mo(W) – Se distance of 2.54 Å. In the electronic structure calculations,

when the spin-orbit coupling is excluded, the spin-up and spin-down valance bands are degenerate at the K point. However, spin-orbit interaction splits these bands from each other by 0.18 eV and 0.47eV at the K point for MoSe₂ and WSe₂ respectively. On the other hand, the spin-orbit interaction at the conduction band minimum is much lower, 0.02 eV for MoSe₂ and 0.03 eV for WSe₂. Here it should be noted that at the K point the valence band maximum is dominated by the $d_{x^2-y^2}$ and d_{xy} orbitals of the Mo/W atoms and the conduction band minimum is dominated by the d_{z^2} orbitals of the Mo/W atom. It should also be noted that the chalcogen atom Se has no contribution to the VBM or CBM at the K point.

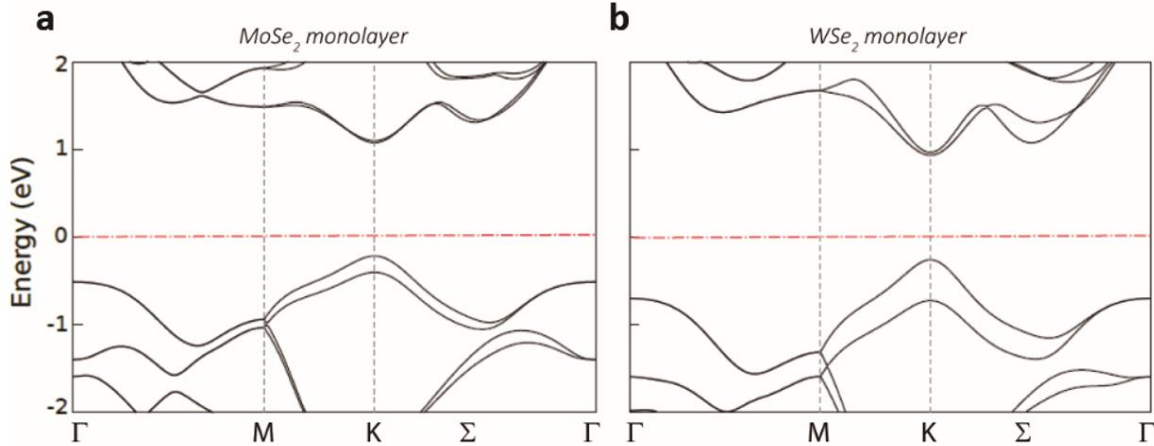


Figure S1 | Computed band structures of single-layer MoSe₂ and WSe₂. **a**, Computed band structure of SL MoSe₂. **b**, Computed band structure of SL WSe₂.

S2. Two interlayer excitons radiative recombination pathways

Figure S2 shows two possible ways to explain a lower energy peak: one is another interlayer exciton (IEX₂) and the other is interlayer trion. As for explanation of another interlayer exciton described in Figure S2a, while IEX₁ occurs at the same momentum space (K-K transition), IEX₂ occurs through pathway placing on different momentum space (K- Σ transition). To make it feasible, the energy variance between the Σ edge at MoSe₂ conduction band and K edge at WSe₂ valence band should be on the same order-of-magnitude as the energy caused by thermal fluctuation. When it comes to explanation of interlayer trion as illustrated in Figure S2b, trions are generated through interaction between interlayer exciton and electron due to electron accumulation in MoSe₂ conduction band minimum on a picosecond timescale [S1,S2]. In effect, we can obtain the trion binding energy (ϵ_T) through the power-dependent photoluminescence. The tuning effect of three-body excitonic system results from the strong quantum-confined Stark effect [S3]. The energy splitting between interlayer neutral exciton and trion is expressed [S4]:

$$\omega_I - \omega_X = E_{Trion} + \Delta E \quad (1)$$

where E_{Trion} is the trion binding energy and ΔE is the energy required for one carrier to be promoted into the free-carrier system. $\omega_I - \omega_X$ denotes the minimum energy for the removal of one electron from the trion, because the exciton is regarded as an ionized trion [S5]. ΔE

becomes negligible when the Fermi surface increases with high carrier injection since the initial doping level (E_F) is less significant as a result of the enhanced carrier screening effect by carrier injection in 2D systems [S6]. In our case, we can expect high quantum PL yield, efficient charge transfer, and large effective mass of the carriers in the trilayer heterostructures. Therefore, ΔE becomes negligible and $\omega_I - \omega_X$ can be taken as the trion binding energy [S4]. In our trilayer heterostructure, trion binding energy is ≈ 27 meV, which deduced from Figure 4b.

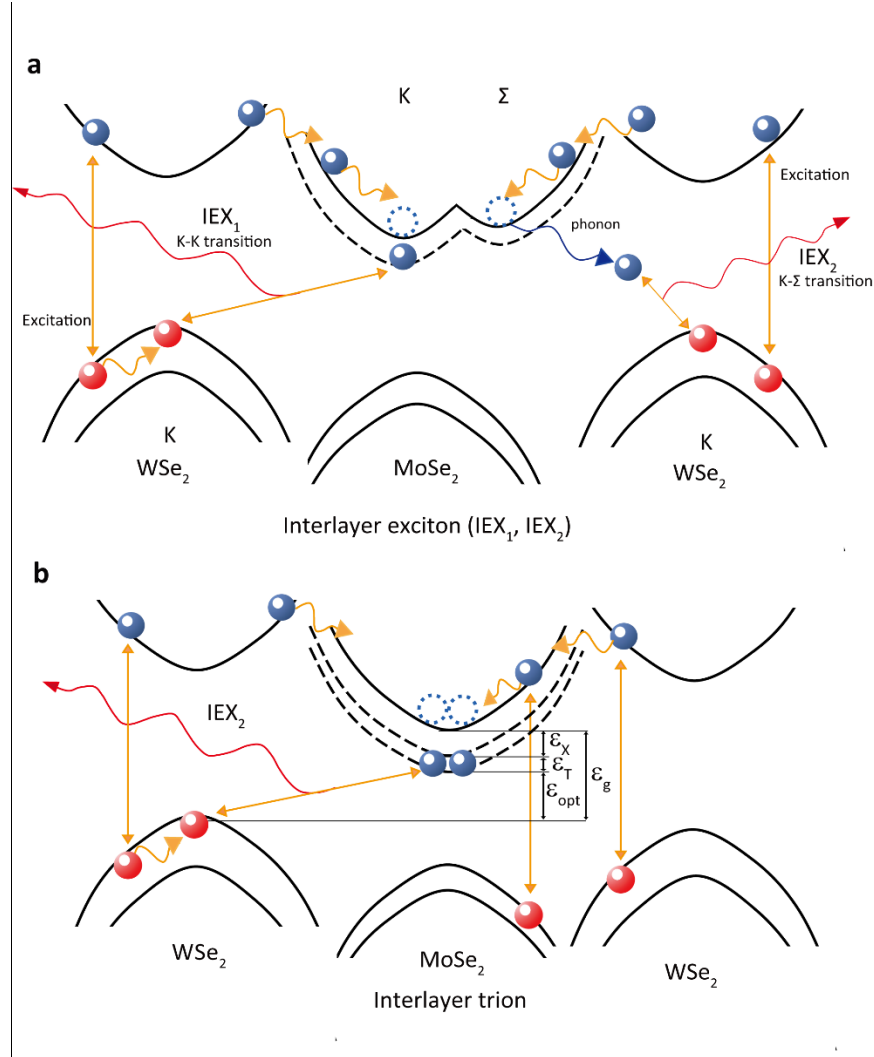


Figure S2 | Illustration of two pathways for interlayer exciton radiative recombination, and the interlayer trions model. a, Illustration of two different interlayer excitons radiative recombination pathways: one is K-K direct transition in k -space and the other is K- Σ indirect transition in k -space. In the case of indirect transitions, phonon is involved to match the momentum difference, which lowers the energy bandgap. **b,** Schematic summary of the interlayer trion radiative recombination predicted by a type-II heterojunction in our trilayer vdWs heterostructure. ϵ_X , ϵ_T , ϵ_{opt} and ϵ_g represent exciton binding energy, trion binding energy, optical bandgap and electronic bandgap, respectively. This is an example in the formation of the interlayer trions: two electrons in MoSe₂ and one hole in WSe₂.

S3. Integrated photoluminescence (PL) intensity in bilayer and trilayer heterostructures

To compare bilayer heterostructure with trilayer heterostructure, integrated PL intensities are measured at ≈ 0.2 mW and with an ≈ 1 μm laser spot size. As shown below, ≈ 3 times brighter PL intensity (and ≈ 30 meV lower energy PL peak) of trilayer heterostructure is observed at 77 K. To show the PL intensity difference of two different heterostructures, we collected the below data in the same bath temperature and excitation time duration by one dimensional InGaAs focal plane array detector. The noise here is caused by the absence of filters, only for this measurement.

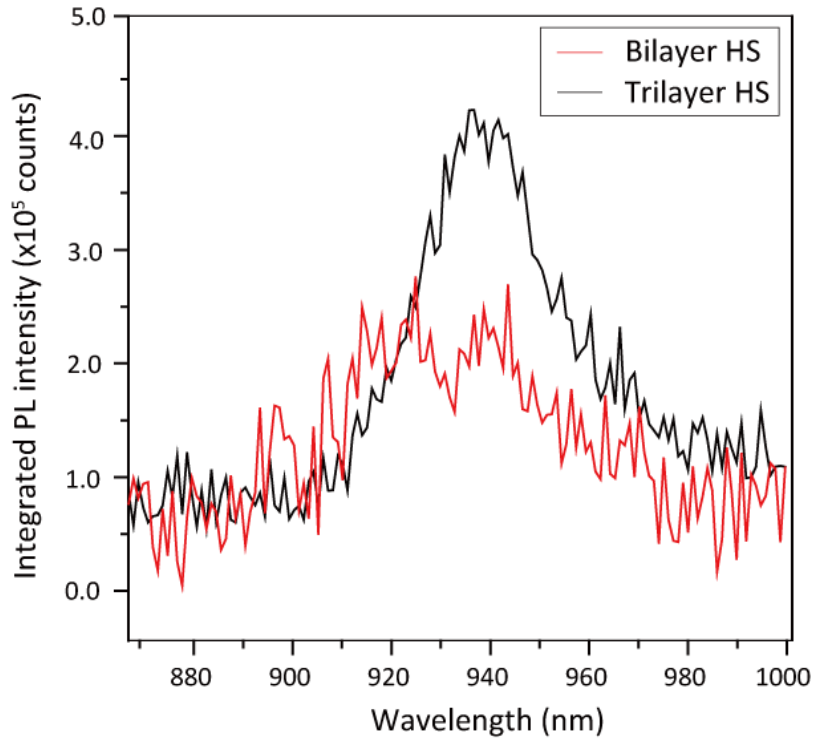


Figure S3 | Integrated PL intensities in bilayer and trilayer heterostructures. This comparison demonstrates the brighter PL emission in $\text{WSe}_2\text{-MoSe}_2\text{-WSe}_2$ trilayer heterostructure than $\text{WSe}_2\text{-MoSe}_2$ bilayer heterostructure, enabled by the tightly overlapping wavefunctions in the trilayer heterostructure.

S4. Full-width half-maximum (FWHM) of two interlayer excitonic states

Figure S4 plots the FWHM of the two interlayer excitonic states. In order to see the temperature effects on the interlayer excitonic states, we extrapolated both sets of FWHM data from Figure 3b and note that IEX_2 features a much broader FWHM than IEX_1 . From 4 K to 96 K, we can see that the FWHM of two interlayer excitonic states is almost constant with increasing temperature, with the interlayer trion (IEX_2) showing a larger width. The tendency of not broadening with increasing temperature suggests that there are more processes, such as defect

scattering or other radiative recombination, contributing to the FWHM other than electron-phonon interactions [S7].

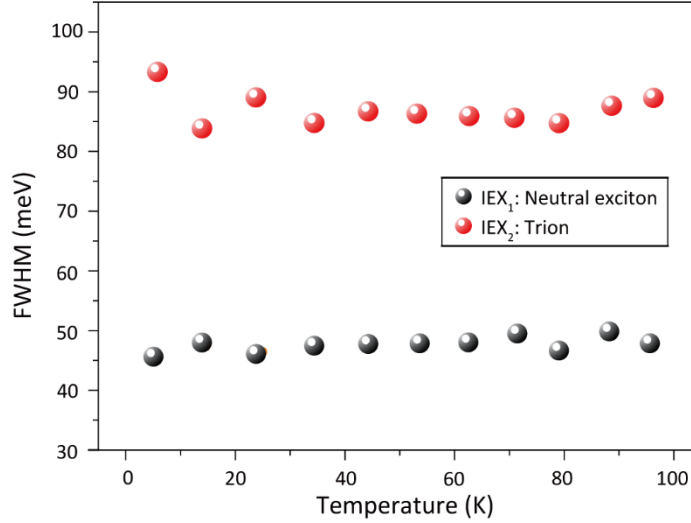


Figure S4 | Full-width half-maximum (FWHM) of two interlayer excitonic states. FWHM of interlayer exciton and trion in the trilayer heterostructure as a function of the bath temperatures.

S5. Semiconductor bandgap renormalization with temperature

In Figure 3c the two PL peaks of excitonic states (neutral exciton and trion) are fitted by temperature-bandgap renormalization model as below [S8]:

$$E_g(T) = E_g(0) - S \langle \hbar\omega \rangle \left[\coth \left(\frac{\langle \hbar\omega \rangle}{2K_b T} \right) - 1 \right] \quad (2)$$

where $E_g(0)$ represents the band gap at zero temperature, S is a dimensionless coupling constant, and $\langle \hbar\omega \rangle$ is an average phonon energy. The above describes the phonon-induced gap reduction with temperature and we fit the neutral exciton peak shift (solid lines in Figure 3c) with corresponding $E_g(0) \approx 1.331$ eV (interlayer neutral exciton ground-state transition energy, 0 K), $S \approx 0.012$ and $\langle \hbar\omega \rangle \approx 9.9$ meV. The trion peak is also fitted by the same values for S and $\langle \hbar\omega \rangle$ parameters but for $E_g(0) \approx 1.284$ eV (interlayer trion ground-state transition energy, 0 K). The energy splitting between the two excitonic states peaks is ≈ 47 meV at 4 K, with 1.96 eV pump and 1.2 mW pump power. It decreases with lower pump power and is ≈ 27 meV at 0.01 mW pump. We focus on the measured data from 4 K to 245 K since above 245 K the PL signals from interlayer neutral exciton and trion become almost indistinguishable from the noise.

S6. Time-resolved photoluminescence (TRPL) with different excitation wavelengths

In addition to the temperature-dependent lifetime measurements, we also performed TRPL measurements by varying the excitation wavelengths to explore the electron-phonon decay

dynamics of the interlayer neutral exciton in the trilayer heterostructure. As shown in Figure S6a, the wavelengths of excitation pulse pump range from 510 nm (green) to 660 nm (red). In each measurement, we selected bandpass filters to exclude the effect of pump side-peaks before our trilayer sample. We further performed TRPL measurements for the interlayer trion; however, its comparably lower photon counts and weaker pump excitation pulse energy below 600 nm does not allow a lifetime to be meaningfully obtained. We also note that our tunable pulse laser has different pulsewidths for different pump excitation wavelengths as shown in Figure S6b. The extracted carrier lifetimes, with a summary shown in Figure S6c, are on the order of nanoseconds and significantly longer than the picosecond pump pulsewidth variations.

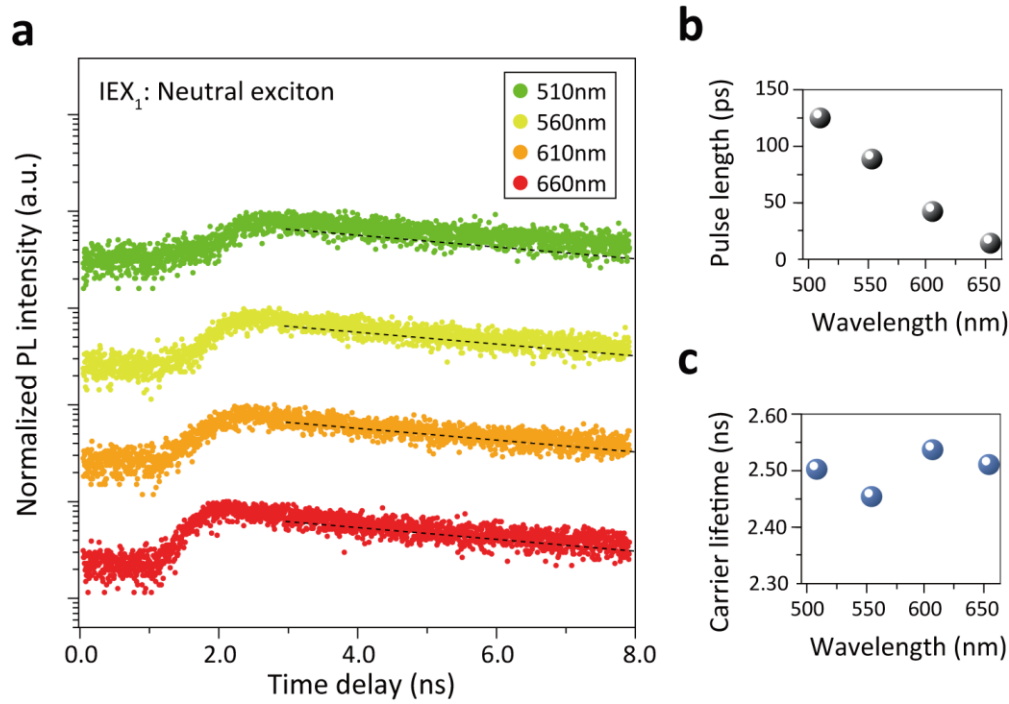


Figure S6 | Carrier lifetimes for various excitation wavelengths. **a**, Interlayer exciton lifetime as a function of excitation wavelengths at 4K. Photoluminescence intensities are normalized and fitted with biexponential decay functions. **b**, Excitation pulsewidths as function of excitation wavelengths, from the pump laser. **c**, Measured carrier lifetimes deduced from panel **a**.

Supplementary References

- S1. Lin, Y., Ling, X., Yu, L., Huang, S., Hsu, A. L., Lee, Y. H., Kong, J., Dresselhaus, M. S., Palacios, T. Dielectric screening of excitons and trions in single-layer MoS₂. *Nano Letters* 2014; **14**: 5569–5576.
- S2. Efimkin, D. K., Macdonald, A. H. Many-body theory of trion absorption features in two dimensional semiconductors. *Physical Review B* 2017; **95**: 035417.

- S3. Miller, D. A. B., Chemla, D. S., Damen, T. C., Gossard, A. C., Wiegmann, W., Wood, T. H., Burrus, C.A. Band-edge electroabsorption in quantum well structures: The quantum-confined stark effect. *Physical Review Letters* 1984; **53**: 2173–2176.
- S4. Jones, A. M., Yu, H., Ghimire, N. J., Wu, S., Aivazian, G., Ross, J. S., Zhao, B., Yan, J., Mandrus, D. G., Xiao, D., Yao, W., Xu, W. Optical generation of excitonic valley coherence in monolayer WSe₂. *Nature Nanotechnology* 2013; **8**: 634–638.
- S5. Mak, K. F., He, K., Lee, C., Lee, G. H., Hone, J., Heinz, T. F., Shan, J. Tightly bound trions in monolayer MoS₂. *Nature Materials* 2013; **12**: 207–211.
- S6. Yang, J., Xu, R., Pei, J., Myint, Y. W., Wang, F., Wang, Z., Zhang, S., Yu, Z., Lu, Y. Optical tuning of exciton and trion emissions in monolayer phosphorene. *Light: Science and Applications* 2015; **4**: e312.
- S7. Molina-Sánchez, A., Palumbo, M., Marini, A., Wirtz, L. Temperature-dependent excitonic effects in the optical properties of single-layer MoS₂. *Physical Review B* 2016; **93**: 155435.
- S8. O'Donnell, K. P., Chen, X. Temperature dependence of semiconductor band gaps. *Applied Physics Letters* 1991; **58**: 2924–2926.